Journal of the Geological Survey of Brazil vol 5, n3, 205 - 220, December 2022

Journal of the Geological Survey of Brazil

Understanding the origin of the airborne geophysical signatures of the Jalapão geomorphological units, Urucuia Basin, Central–Northern Brazil

Adolfo Barbosa da Silva[1*], Felipe da Mota Alves[1]

[1]Geological Survey of Brazil. Rua 148, 485, Goiânia-GO, Brazil, CEP: 74170-110

Abstract

This study was carried out in order to understand the airborne geophysical signatures observed in the Jalapão region, Urucuia Basin, eastern Tocantins state. Airborne geophysical data (magnetic and gamma-ray spectrometry) and satellite images (Advanced Spaceborne Thermal Emission and Reflection Radiometer – ASTER) were processed and interpreted. I It was possible to characterize the main geomorphological units of the Jalapão region (residual landforms and dissected surfaces). The residual landforms (e.g., Serra do Espirito Santo and Occidental Bahiano Plateau) have high concentrations of equivalent U (eU) and equivalent Th (eTh), and low K concentrations. ASTER image analysis suggests that these concentrations can be correlated with the products of chemical weathering (Fe oxides, clay, and weathering-resistant opaque minerals and other accessories). The dissected surfaces (mainly Jalapão Surface), however, is deficient in these radioelements, probably due to the quartz-rich nature of the related soils. Furthermore, the Jalapão Surface is practically non-magnetic, whereas residual landforms exhibit magnetic signals of low amplitude and high frequency, and are of unknown origin. The results suggest that the sources of these magnetic anomalies are shallow (≈ 270 m) and could be associated with ferrimagnetic minerals present in the alteration zone and/or in the ferruginous cements of the Serra das Araras Formation sandstones. The depth to basement in the region of this basin (1.44 km) rules out the possibility that the magnetic sources could be related to residual landforms.

Article Information

Publication type: Research Papers
Received 8 September 2022
Accepted 3 November 2022
Online pub. 4 November 2022
Editor: Vladimir Medeiros

Keywords:
Airborne geophysics,
ASTER satellite imagery,
Residual landforms,
Jalapão Surface,
Geomorphology

*Corresponding author
Adolfo Barbosa da Silva
adolfo.barbosa@sgb.gov.br

1. Introduction

Weathering and erosion are exogenous processes that act in the evolution of a landscape and in the development of relief on the earth's surface (Turkington et al. 2005). Such processes have contributed to a number of human activities, such as the mineral industry or the geotourism sector - the latter through the formation of relief forms of scenic beauty.

The Brazilian territory exhibits a wide variety of relief forms of outstanding natural beauty (Vieira et al. 2015). Major examples are the Chapadas dos Guimarães, Veadeiros, and the tablelands around the city of Diamantina. In the eastern part of Tocantins State in northern Brazil, the Jalapão region has developed into a tourist hub of great potential (ICMBio 2013).

The Jalapão region (Figure 1) denotes a part of the cliffs, rivers, and tributaries of the Tocantins-Araguaia watershed in Tocantins State. The name "Jalapão" is derived from one of the most common plants in the Cerrado, Jalapa, which is found in the region (NATURATINS 2003). The effects of the alternating dry (May to September) and humid (October to April) seasons on the region's lithologies have resulted in the receding escarpments of the Serra Geral and Chapada das Mangabeiras, since the Cretaceous. Thus, the geomorphology of this region is testimony for the regional natural history, in the form of diverse residual landforms (Benvindo 2009; Dutra et al. 2008; Morais and Cristo 2015; NATURATINS 2003).

In regional airborne geophysical anomaly maps, the Jalapão region is seen with smooth magnetic relief and a low intensity radiometric pattern (Correa 2019a, 2019b) (Fig.1a and 1b). Such responses are a direct reflection of the limited lithological variability in this region, with rocks mostly composed of sandstones of the Urucuia Group. However, more detailed analysis leads to the recognition of some high-frequency magnetic anomalies that contrast with regional patterns (Silva and Alves 2021) (Figs. 1c and 1d). Such anomalies seem to be closely linked to residual landforms, but so far the possible correspondence between these

ISSN: 2595-1939
https://doi.org/10.29396/jgsb.2022.v5.n3.4
Open access at jgsb.cprm.gov.br

features has not been addressed yet. Moreover, the residual landforms are also noted on radiometric images (Figs. 1a and 1c), but the relation between gamma-ray and residual landforms in the Jalapão region is still unknown.

Understanding the origin of these contrasting responses may provide clues to the genesis of residual landforms and explain geophysical anomalies in the region. We have processed and interpreted data from several remote sensors (magnetic, gamma-ray spectrometry, and ASTER satellite imagery) with the aim to characterize the geomorphological units of the Jalapão region and discuss their possible origin.

2. Geologic Setting

The study area is located in the northern part of the Late Cretaceous Urucuia Basin (UB) (also known as Espigão Mestre), a large sedimentary basin with approximately 790 km - length and 170 km- width located at western edge of the São Francisco Craton, in central-northern Brazil (Fig. 2). The UB is a subsystem of the northern portion of the Sanfranciscana Basin, which is predominantly filled by sandstones of the Urucuia Group (Campos and Dardenne 1997a).

The UB depression is believed to have formed during the transition from the rift to post-rift transitional phase of the Atlantic Ocean during the Late Cretaceous. At this stage, intraplate stresses would have induced additional subsidence in a preexisting flexural basin at the western edge of the São Francisco Craton, thus enabling the deposition of Urucuia Group fluvial-eolian sandstones on top of eolian Areado Group sandstones (Chang et al. 1992; Sgarbi et al. 2001; Spigolon and Alvarenga 2002). Structurally, the southern limit of the UB is marked by the Paracatu High (PH) and the northern limit by the São Francisco Arch (SFA) (Campos and Dardenne 1997a; Sgarbi et al. 2001) (compare Fig. 2).

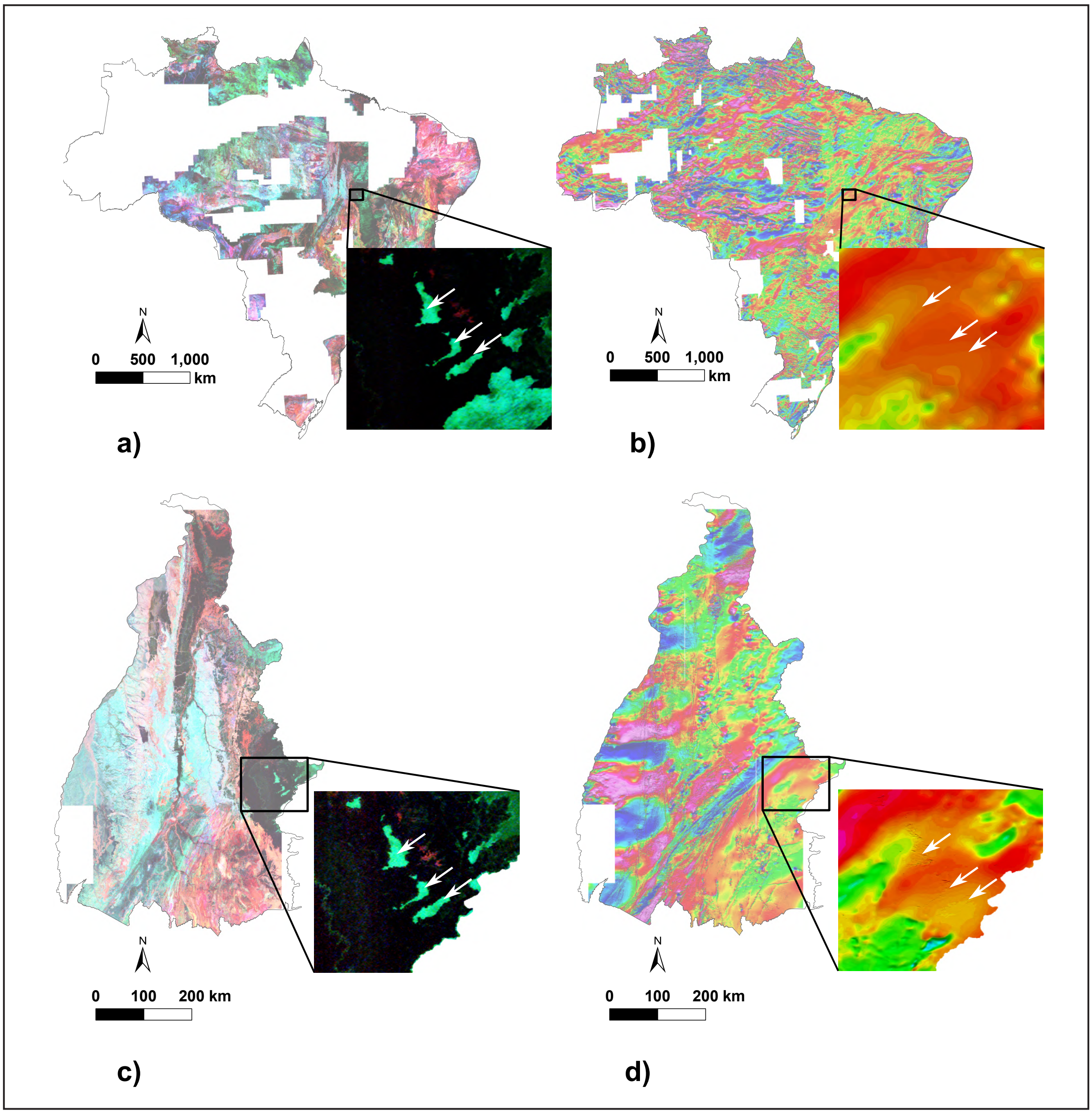

FIGURE 1 – Airborne geophysical maps''. Brasil 's radiometric (a) and magnetic (b) maps. Modified from Correa (2019a, 2019b). Tocantins States' radiometric (c) and magnetic maps (d). Modified from Silva and Alves (2021). The highlighted area on each map denotes the Jalapão region. The white arrows indicate the residual landforms.

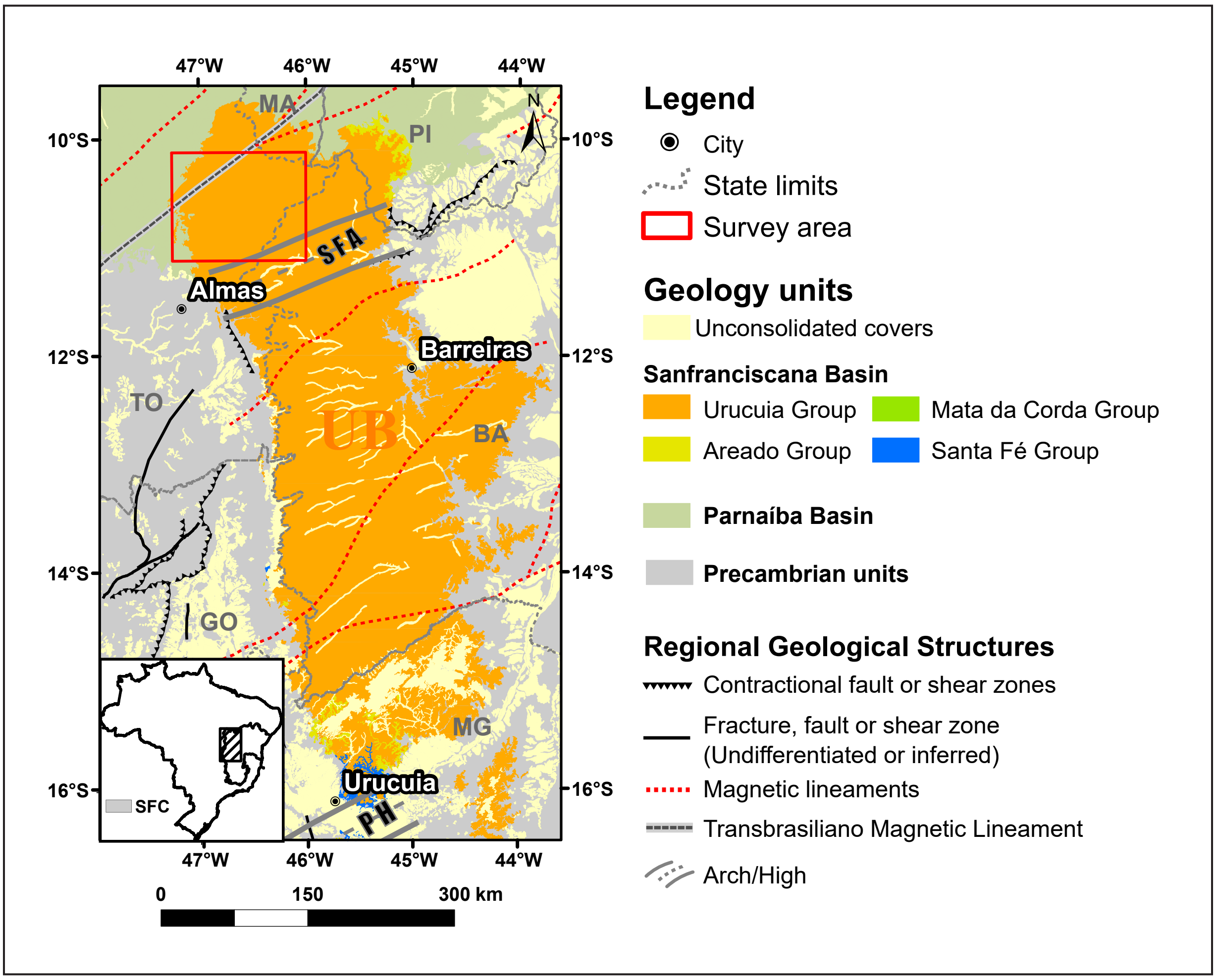

FIGURE 2 – Simplified regional geological map of the Urucuia Basin (UB) showing its location in relation to the São Francisco Craton (SFC) and the survey area. SFA – São Francisco Arch. PH – Paracatu High. Federative units of Brazil: Bahia (BA); Tocantins (TO); Minas Gerais (MG); Piauí (PI); Maranhão (MA). Source of Geographic Information System (GIS) files: Serviço Geológico do Brasil - CPRM (2021).

The Urucuia Group is comprises a sandstone successions that is divided into the Posse and Serra das Araras Formations (Fig. 3). The Posse formation is subdivided into two Facies: Facies 1 - composed of sandstones with a predominance of quartz and limited proportions of chert, feldspar, polycrystalline quartz, zircon, and tourmaline, and epidote; Facies 2 - composed of feldspathic sandstones and quartz sandstones with epidote, zircon, tourmaline, and opaques as accessory minerals. The Serra das Araras formation is composed of quartz sandstones, conglomerates, and claystones, with a predominance of quartz grains, and subordinate tourmaline and zircon. Although cementation by silica and iron oxides occurs widely in both formations, it is so intense within the sandstones of the Serra das Araras Formation that the rock loses its primary characteristics and resembles a chert (silexite) (Campos and Dardenne 1997b; Sgarbi et al. 2001; Spigolon and Alvarenga 2002).

In the study region, the Urucuia Group is overlain sandstones, siltstones, shales and conglomerates of the Neocarboniferous – Eotriassic Sequence (Balsas Group) of Parnaíba Basin (Morais and Cristo 2015; Vaz et al. 2007). The upper and lower portions of this sandstone package show whitish and reddish colors due to cementation by silica and iron oxides, respectively (Cristo et al. 2013; Morais and Cristo 2015). This cementation has provided greater cohesion to the sandstones, making them more resistant to exogenous degradation, so that differential erosion resulted in a scenario where the geomorphological compartments is represented basically by dissected surfaces and residual landforms (Mendes 2008) (Fig. 4).

The residual landforms are represented by buttes, mesas, pinnacles, and plateaus, with sloping scarps and flat tops which soils are mainly composed of laterites (Fig. 4). These landforms are located at topographic levels between 770 and 798 m altitudes and are supported by sandstones. The desagregation these sandstones have driven the deposition of sediments into dissected surfaces. These surfaces are represented by Jalapão and Ponte Alta do Tocantins Surfaces (Fig. 4). They occur at below 500 m altitude, are flat, and their soils are basically comprises of Quartzarenic Neosols. Besides well-known tourist attractions related geomorphological features (ICMBio 2013), the Jalapão's region has also attracted the attention of researchers in the hydrogeology and paleosoil fields.

Hydrogeology researchers have highlighted the role of the Jalapão residual hills as main interfluves of two of the main Brazilian hydrographic watersheds (Tocantins and São Francisco) (Villela and Nogueira 2011). Moreover, the Jalapão residual hills are also recharge zones for the Urucuia Aquifer System which has been the subject of several geophysical studies (Bonfim and Gomes 2004; Gaspar et al. 2012; Kiang and Silva 2015; Tschiedel 2004; Amorim Junior and Lima 2007; Gonçalves et al. 2020). Gaspar (2006) carried out two vertical electrical soundings (VES's) with the electromagnetic method in the time domain to estimate the thickness of the Urucuia Group (Fig. 4). According to this geoelectric model, layers with higher resistivities (15,000 – 60,000 Ω) and interfaces at 270 m are attributed to the Urucuia Group sandstones, whereas resistivity between 8,000 and 24,000 Ω at an interface at 1.4 km depth is attributed to basement rocks.

Regarding paleo soil research, Bueno (2012) identified two paleo soil profiles in the Serra das Araras Formation, one of which is located at the top of the Serra do Espírito Santo (Fig. 4). According to this author, red and unconsolidated deposits, some of which are ferrugenous, with many nodular ferricrete occurrences also occur at the top of the Serra do Espírito Santo. In such outcrops, argillaceous materials are also present.

3. Methodology

3.1 ASTER satellite image processing

The satellite images used are derived from Advanced Spaceborne Thermal Emission and Reflection Radiometer (ASTER) sensor which comprises three radiometers that capture solar radiation reflected and emitted by the Earth's surface in three sections of the electromagnetic spectrum: visible and near infrared (Visible and Near – Infrared Region – VNIR); short wave infrared (Short Wave Infrared Region – SWIR), and Thermal Infrared Region (TIR) (Fujisada 1998). These wavelength regions are divided into 14 spectral bands: 1 to 3 (VNIR); 4 to 9 (SWIR), and 10 to 14 (TIR). The spatial resolutions for the bands are 15 m (VNIR), 30 m (SWIR) and 90 m (TIR). All bands have eight-bit radiometric resolution. For this study only the bands from the VNIR and SWIR subsystems were used.

The scenes used were generated on 1 June 2001 with cloud coverage below 3% (Product Id: AST_L1T_00303022

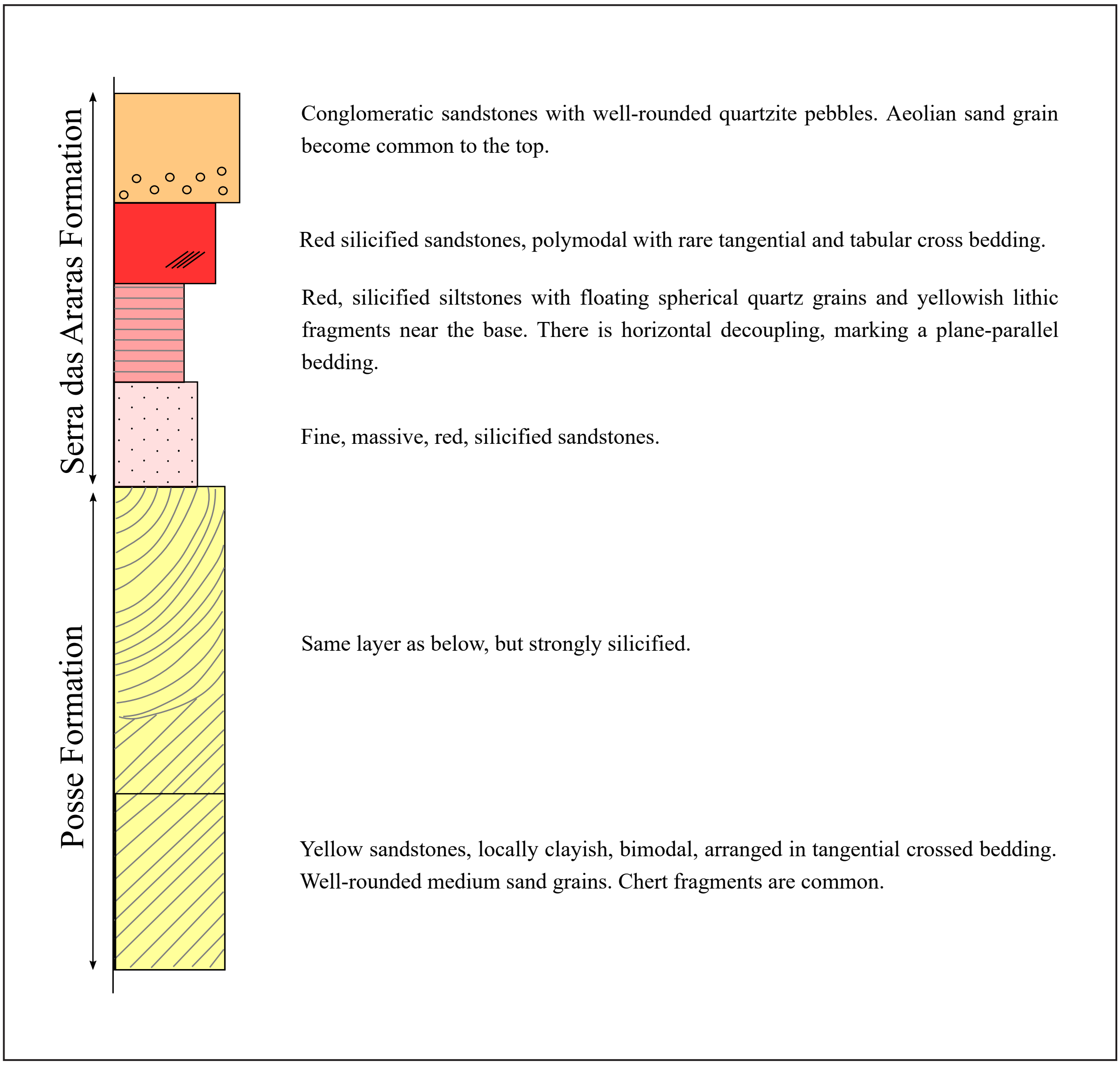

FIGURE 3 – Simplified stratigraphic column of the Urucuia Group based on field studies by Bueno (2012) and lithological descriptions by Campos and Dardenne (1997a). Modified from Bueno (2012).

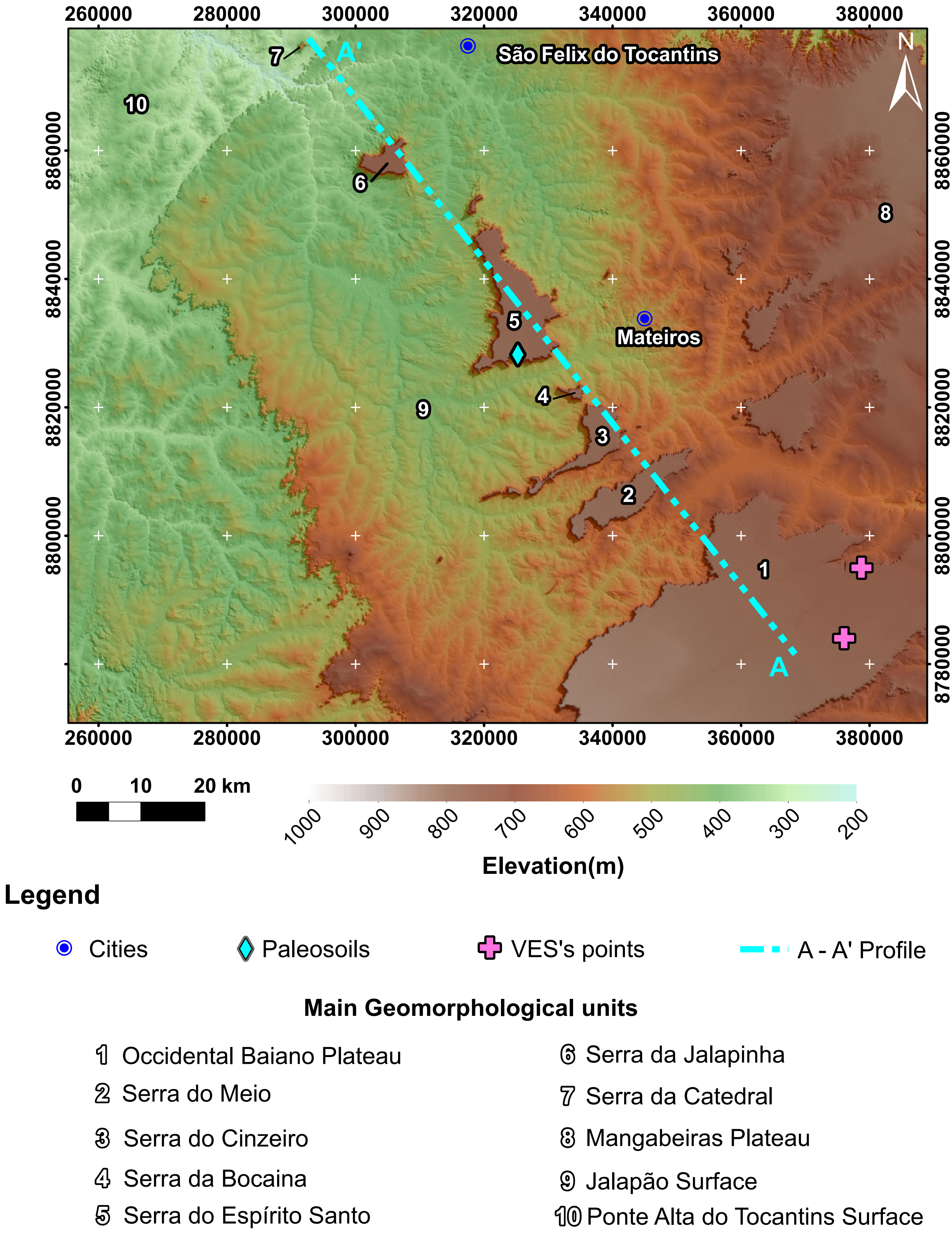

FIGURE 4 – Elevation map of survey area showing geomorphological units and geoscientific investigation sites. The Digital Elevation Model was derived from the Shuttle Radar Topography Mission (SRTM). VES's point = Localization where Gaspar (2006) carried out vertical electromagnetic soundings. Paleosoil = Localization where Bueno (2012) carried out paleosoil field surveys.

001133959_20150116101825_52811 and AST_L1T_00306 022001133950_2015041601824_52757). The images were pre-processed by the Land Processes Distributed Active Archive Center (LP DAAC) team and then made available on the USGS Earth Explorer platform (LP DAAC 2020). The image processing level is L1T, which includes radiometric, geometric, cross-talking, terrain accuracy, and north rotation corrections. The scene data contain the radiance calibrated in the sensor, with the values stored in the form of digital numbers (LP DAAC 2020).

The ASTER L1T images were downloaded from the Earth Explorer platform and imported into the L3Harris Geospatial ENVI 5.5 software (Fig. 5). The digital numbers were converted to radiance values calibrated in the sensor and, later, the VNIR and SWIR bands were atmospherically corrected using the Quick Atmospheric Correction (QUAC) module (ENVI 2009).

The VNIR bands were resampled to 30 m resolution and combined with the SWIR bands in a multi-band raster. The VNIR–SWIR layer raster was used to produce colored RGB compositions and spectral profile charts. For both products, we chose to present the results only for the Serra do Espírito area because the main spectral features highlighted more important geological features.

The RGB color composite of individual (B6, B3 and B1) bands and band ratios (B4/B3, B2/B1 and B6/B4) were produced after applying the Decorrelation Stretch transformation (Kalinowski and Oliver 2004). These compositions were chosen because they are useful in the recognition of soils derived from weathering (Deller 2006). The compositions were superimposed onto a shaded relief map (obtained as explained in the next section) and later organized into maps in the Geographic Information System (GIS) environment.

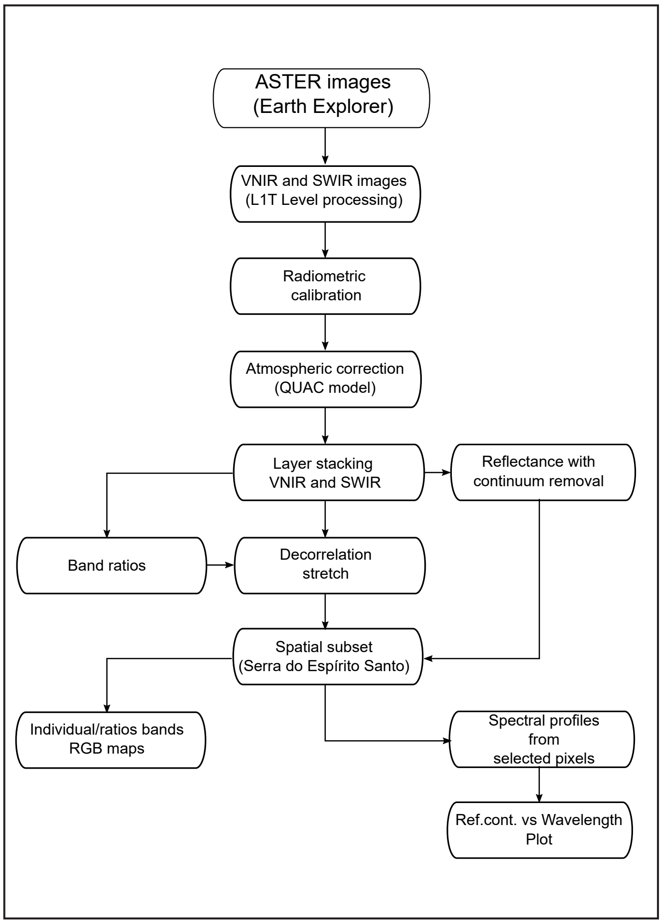

FIGURE 5 – Flowchart for the processing of ASTER sensor images.

During processing, areas with different shades within the Serra do Espírito Santo regions were identified on the RGB maps. To investigate these areas in more detail, five points (ES01 – ES05) were selected to extract spectral profiles from pixels. ES04 and ES05 points coincide with the paleo soil location profile identified by Bueno (2012) and with Jalapão dune deposits described by Morais and Cristo (2015), respectively. To facilitate the visualization of the absorption features, the reflectance of the VNIR – SWIR layer was transformed from 0 to 1 by applying a Continuum curve (Clark and Roush 1984). Then, the reflectance with continuum removal values of the pixels located at the points were extracted and organized in a chart.

3.2 Airborne geophysical data processing

The airborne geophysical data used here were acquired and pre-processed in 2005 and 2006. The data were made available by the National Agency of Petroleum, Natural Gas and Biofuels (ANP). The flight and ties line spacings were 0.5 km in the NS direction and 4 km in the EW direction, respectively (Marques et al. 2006). In the pre-processing stage, the following corrections were applied: parallax, removal of diurnal variation, removal of the International Geomagnetic Reference Field (IGRF), leveling and micro-leveling for the magnetic data, and dead time, background removal (aircraft, cosmic and atmospheric radon), height, Compton Effect, and conversion to elemental concentrations for the gamma-ray spectrometric data.

In the post-processing step shown in the flowchart of Figure 6, the software Oasis Montaj 9.8.1 from Seequent was used to obtain grids of the Anomalous Magnetic Field (AMF) and the radioelement concentrations (K, eTh and eU) through interpolation (125 m cell size) of the airborne geophysical data by the Bi–Directional and Inverse Distance Weighted (IDW) methods, respectively.

The concentration grids were imported into the GIS environment, where they were organized into maps. The concentration grids are also used to produce an RGB composite color map with K in the red band, eTh in the green band, and eU in the blue band. These radiometric maps were superimposed onto a shaded relief map, which was calculated from a 30 m resolution digital terrain model (DEM) derived from the Shuttle Radar Topography Mission (SRTM). The shaded relief topography was calculated considering a light source with an elevation and azimuth of 45°.

During the magnetic data processing stage, there was a need to perform the regional-residual separation of the AMF to highlight the high-frequency magnetic anomalies. This task was performed through the analysis of the Radially Averaged Power Spectrum (RAPS) and Gaussian filtering.

According to the methodology proposed by Spector and Grant (1970), the AMF of a given area can be considered the result of the superposition of various magnetic anomalies generated by sets of prismatic bodies arranged side by side. Based on this approximation, it is possible to calculate the RAPS for all prismatic bodies and identify the different contributions of the magnetic signal due to different ensembles

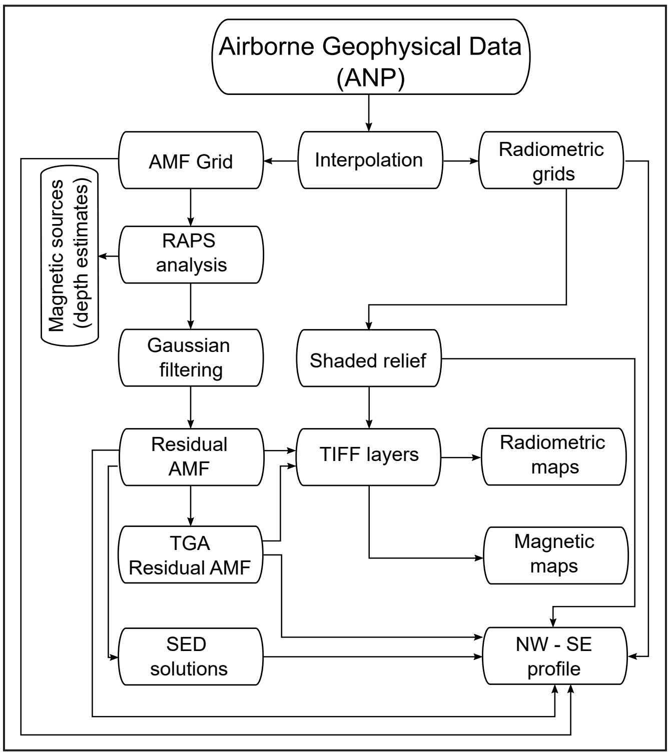

FIGURE 6 – Flowchart for the processing of airborne geophysical data.

(set of magnetic sources) (Spector and Grant 1970). As average depth of the ensemble strongly influences the RAPS curve, a change in this parameter modifies the RAPS decay rate curve.

For a theoretical magnetic source with infinite depth, RAPS decay rate approximates a straight line, whose slope is directly proportional to the average depth of the ensemble. In the case of real data, the magnetic signal is composed of many sources at different depths; even so, a simple linear regression can be fit at different intervals of the RAPS decay curve. The wavelength separating the straight regression lines can be used to separate the regional and residual components of the AMF, whereas the slope of the lines can be used to estimate the average depth of the identified ensemble.

Using the MAGMAP tool integrated in the Oasis Montaj software, this study calculated the RAPS curve from the results of the Fast Fourier Transform on the AMF grid. From the analysis of this curve, it was possible to identify three magnetic sources in the ensemble, called S1, S2 and S3 (Fig. 7). Table 1 presents the parameters of this linear regression model, as well as the depths estimated from the angular coefficients.

In order to enhance the magnetic signals from shallow sources (S3), a Residual Anomalous Magnetic Field grid (RES - AMF) was obtained from the application of a residual Gaussian filter with a wavenumber of 0.53 rads/km (equivalent to the wavelength of ca. 1880 m) over the original AMF grid. Then, the Total Gradient Amplitude (TGA) (also known as Analytical Signal Amplitude) (Roest et al. 1992; Li 2006) was calculated from the RES – AMF grid. Similarly, the magnetic grids were organized into maps in a GIS environment.

In order to better evaluate the airborne geophysical responses and their respective associations with residual landforms, the radiometric (K, eTh and eU), magnetic (AMF, RES – AMF and TGA), and DEM data were sampled with the same spacing (125 m) for a profile A – A' shown in Fig. 4. This profile also includes other depth estimates derived from the Standard Euler Deconvolution Solution (SEDS) method described below.

The magnetic anomaly depth information can also be gained from the SEDS. RAPS and SEDS estimate the depth of magnetic sources independently of the magnetic susceptibility contrast (Li 2003). However, whereas RAPS graphical analysis provides an average depth for a given magnetic source ensemble without spatial location, each SEDS is represented by the coordinates of each anomalous magnetic source (x, y and z) (Barbosa and Silva 2005).

In the SEDS approach, each magnetic anomaly is assumed to have simple ideal geometries according to its structural index

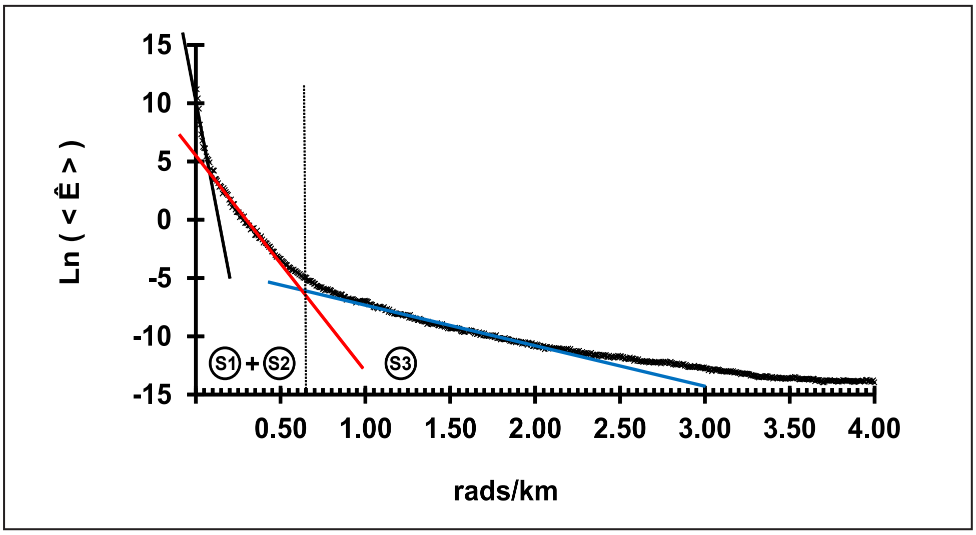

FIGURE 7 – Radially Averaged Power Spectrum (RAPS) plot derived from the AMF of the investigated area. The straight lines in black, red and blue correspond to simple linear regressions fit to the decay curves at ensembles S1, S2 and S3, respectively. The vertical dotted line corresponds to the wavenumber that separates sources S1 and S2 from source S3.

TABLE 1: Linear fitting parameters for the identified magnetic sources

Ensemble	Coeff. α	R^2	Depth (km) {h = (- α / 4π)}
S1	- 85.931	0.90	6.83
S2	-18.144	0.99	1.44
S3	-3.455	0.98	0.27

(η). This index corresponds to the rate at which the magnetic signal decays with source–sensor distance (Barbosa and Silva 2005). For simple geometries such as a straight contact, vertical dike or sill, vertical or horizontal cylinder, or sphere, the value of η assumes 0, 1, 2, and 3, respectively (Barbosa and Silva 2005; Reid et al. 1990; Thompson 1982). Once η and the size of the datas´ moving window are defined, the SEDS are calculated by linear inversion (Li 2003).

In this work, the RES – AMF values sampled along the A – A' profile were imported into the EUDEP program by Durrheim and Cooper (1998) to calculate the SEDS. In the settings of this program, the inclination, declination, and total field of the geomagnetic field were obtained through the magnetic calculator available on the website of National Center for Environmental Information (NCEI) of the National Oceanic and Atmospheric Administration (NOAA) (NCEI 2021). This calculator uses the Enhanced Magnetic Model 2017 to calculate the geomagnetic components for a given date, location and elevation. For the purpose of this study, the approximate acquisition date for this airborne geophysical survey (06/01/2006) and the location of the town of Mateiros, which average elevation of 550 m, were considered. The other parameters are shown in Table 2.

4. Results

Analysis of the maps obtained in this study reveals that the residual landforms have different airborne geophysical and spectral character from the surrounding terrain (Jalapão Surface). Residual landforms are well distinguished in the RES – AMF and TGA images, but not on the AMF image (Figs. 8 and 9). This demonstrates that the filtering process was adequate to separate high and low frequency components. The effectiveness of the filter can also be observed when comparing the AMF and RES – AMF curves in profile A – A' (Fig. 10).

TABLE 2: Input parameters for the application of the EUDEP program.

Parameters	Values
Total Field	24516.4 nT
Declination	-21.0636°
Inclination	-16.1052°
Profile inclination	140°
Flight height	100 m
Structural Index	1.00
Window size	1875 m
X/Y Separation	125 m
Maximum depth	3500 m

In this profile a good correlation between the topographic profile of the residual landforms and the TGA curve is noted as well. Based on the TGA curve, it is possible to characterize the Jalapão Surface as essentially non-magnetic. Residual landforms also have a weak magnetic signal, but there is a good positive correlation between TGA > 0.004 nT/m and the edges of these landforms (Fig. 10).

The depth estimates of magnetic sources obtained by the SEDS method show that the aforementioned TGA values coincide with mainly shallow depths (< 400 m). In contrast, magnetic source depths for the surrounding terrain vary between 600 and 1000 m. Regarding the depths estimated by the RAPS analysis, the estimate of average depth ensemble S3 (~ 0.27 km) is similar to values obtained by vertical electromagnetic soundings (VES) (270 m) for the Urucuia Group. The values for the depths to basement estimated by VES (~ 1.4 km) and for ensemble S2 (1.44 km) are also in agreement with each other, but it was not possible to compare

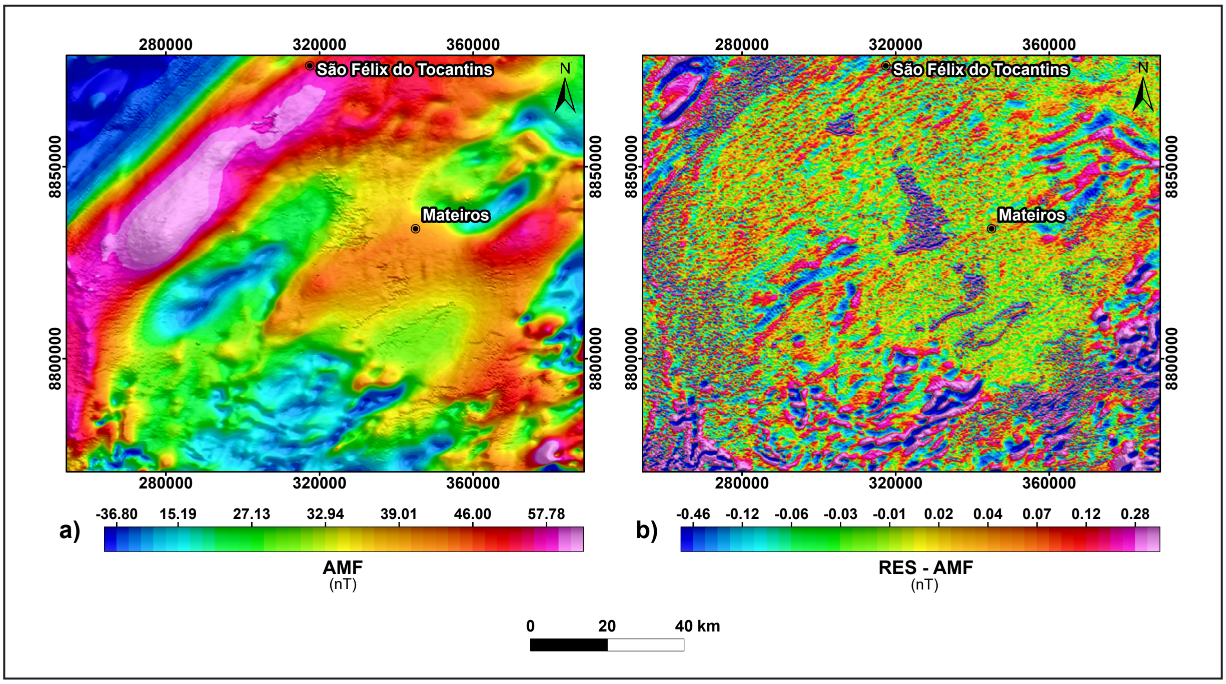

FIGURE 8 – Magnetic maps. a) Anomalous Magnetic Field (AMF). b) Residual Anomalous Magnetic Field (RES – AMF).

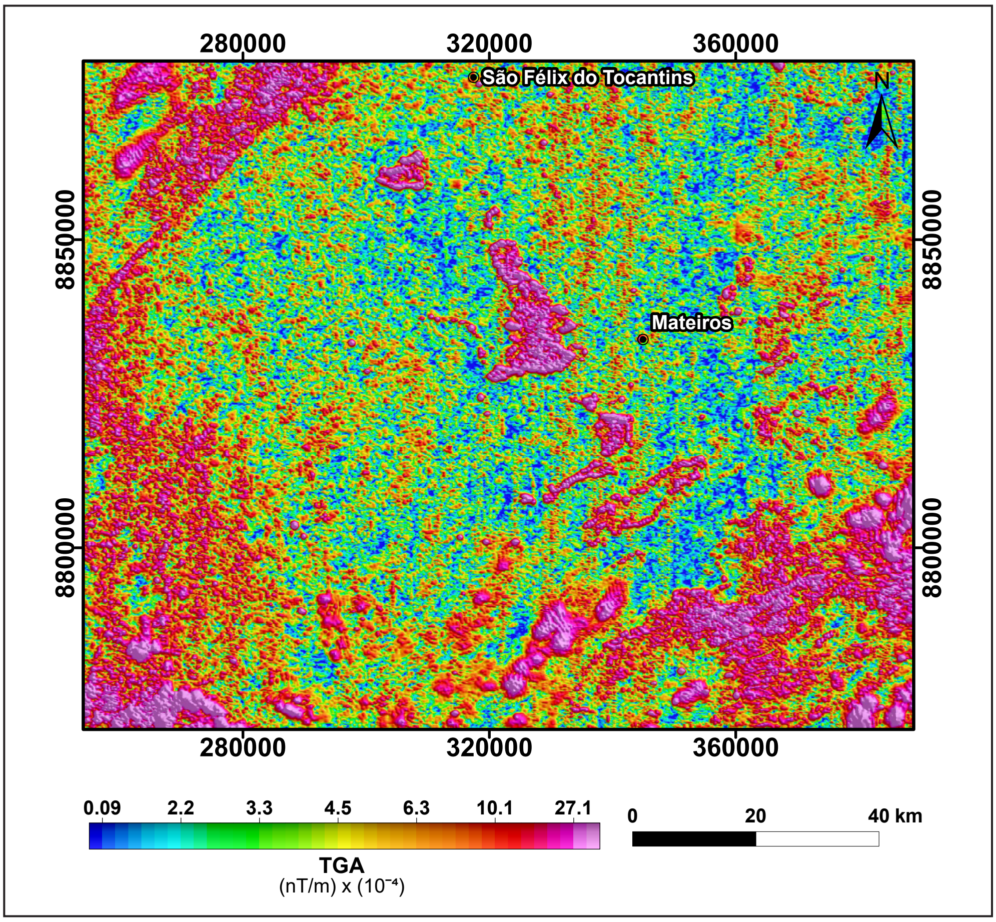

FIGURE 9 – Total Gradient Amplitude Map (TGA)

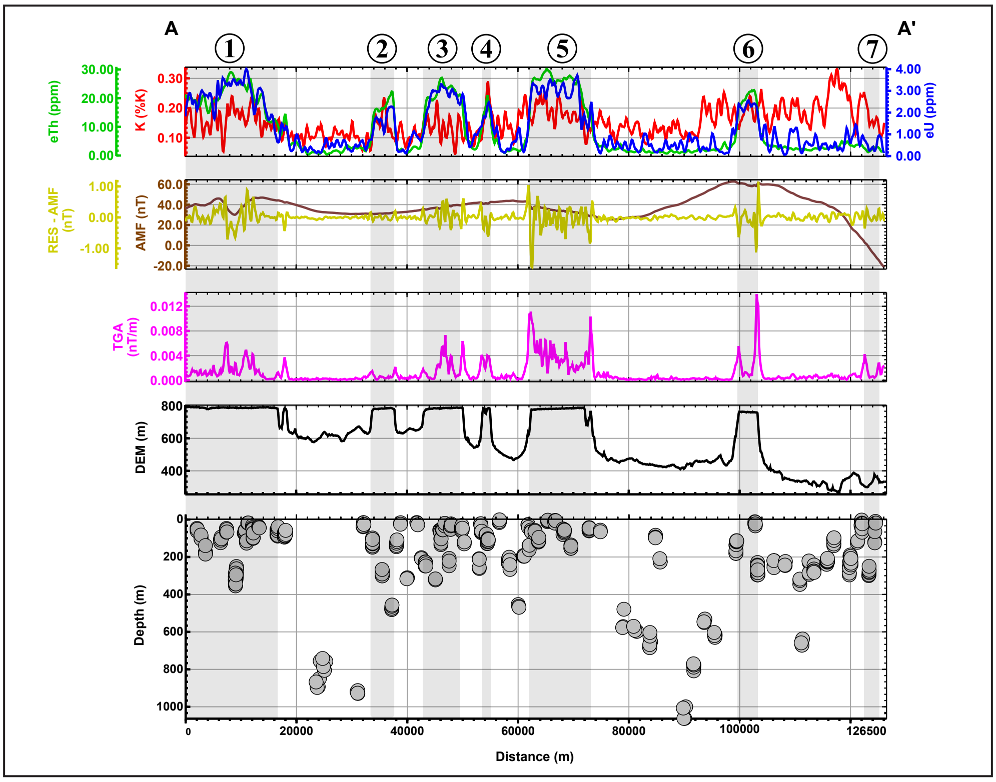

FIGURE 10 – Profile A – A' (compare Figure 1). Residual landforms: 1 – Occidental Baiano Plateau; 2 – Serra do Meio; 3 – Serra do Cinzeiro; 4 – Serra da Bocaina; 5 – Serra do Espírito Santo; 6 – Serra da Jalapinha; 7 – Serra da Catedral.

the depth to ensemble S1 (~ 6.83 km) with other studies carried out in the region.

Residual landforms can also be separated from Jalapão Surface based on airborne gamma-spectrometry signatures (Fig. 11). The Jalapão Surface is visibly depleted in K, eTh and eU, being represented by vast dark areas in Figure 11d. However, small areas with reddish hues, with concentrations of up to 0.6 % K, occur over the eastern portion of the Serra do Espirito Santo, mainly along the main river (Ribeirão Brejão), and around the towns of Mateiros and São Félix do Tocantins (Fig. 11a and 11d).

The residual landforms are characterized by high eU (> 3 ppm) and eTh (> 20 ppm) and low K (< 0.20%) concentrations, resulting in a strong cyan hue in the RGB map (Fig. 11d). Profile analysis shows that K concentration values greater than 0.2 % seem to be more frequent on the top of mesas and plateaus, mainly over the Serra da Bocaina and Serra do Espírito Santo (Fig. 10).

Figure 12 shows the RGB composite color for ASTER sensor images (individual bands and ratios) and Figure 13 the spectral profile from extracted pixels based on the ES01 to ES05 points. To facilitate the process of interpretation and

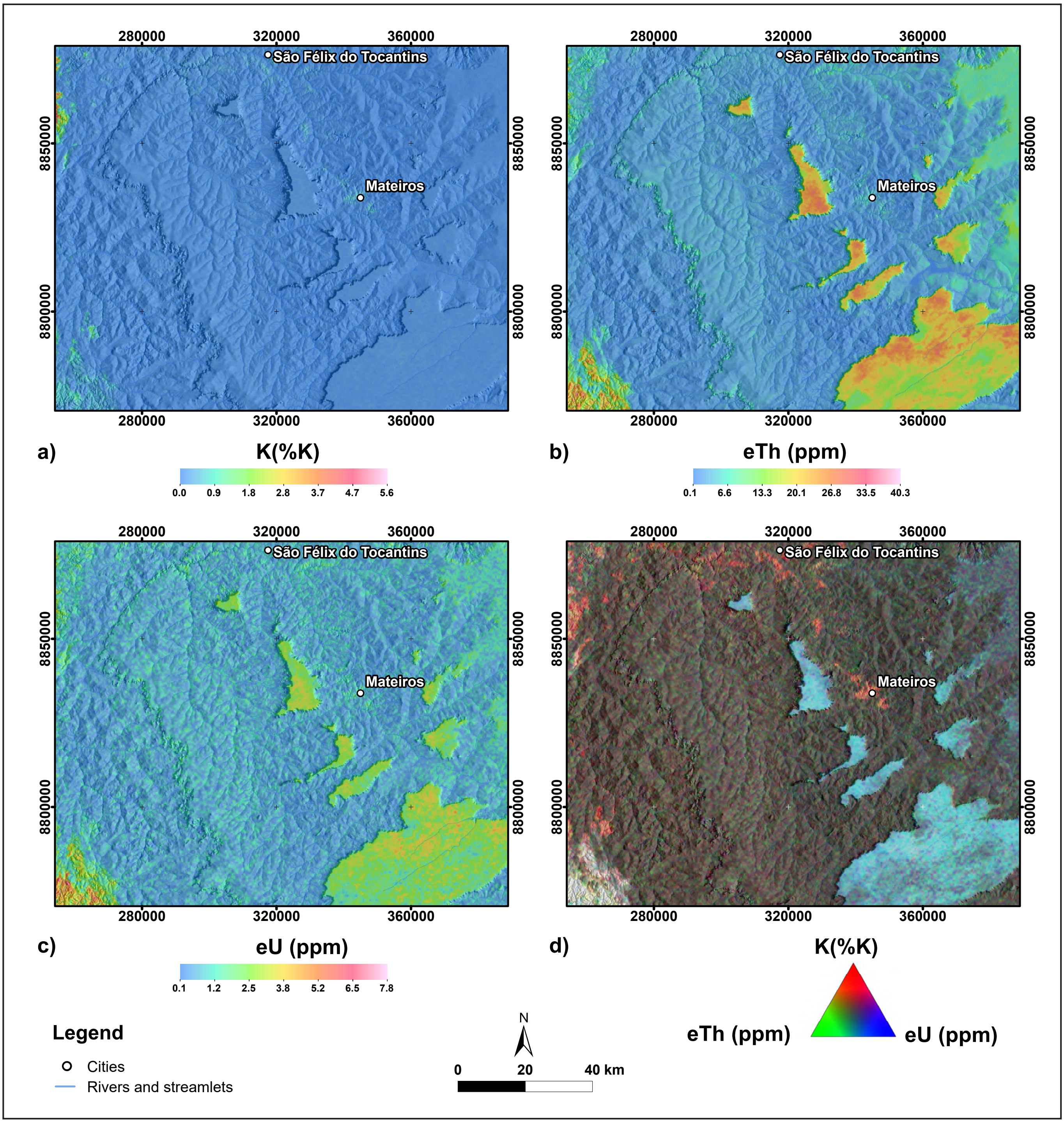

FIGURE 11 – Radiometric maps. a) K percentage ; b) Th equivalent; c) U equivalent; d) RGB composite color with K in the red band, eTh in the green band, and eU in the blue band.

discussion of results, a description of the shades of the areas represented by the ES01 - ES05 and the main absorption features observed at these points are summarized in Table 3. For example, areas represented by the ES01 point are depicted in olive green (RGB individual bands) and aqua green (RGB ratios) tones, and the main absorption features occur at 0.66 μm and in the range from 2.17 to 2.21 μm. The same is observed for ES02 to ES05.

5. Discussion

The geomorphological units of the Jalapão region are covered by lateritic and quartzose – sandy soils, respectively. Considering that the signals captured by the gamma-spectrometric and ASTER sensors derive from surface materials (< 1 m depth), it is likely that the signals of these sensors are related to the composition of these types of soils.

It is known that the chemical weathering process tends to favor the concentration of Th and U, either due to the incorporation of these elements in Fe oxides or due to their concentration in weathering-resistant minerals such as zircon and tourmaline (e.g., Reinhardt and Hermann 2018; Wilford and Minty 2007). On the other hand, K tends to be leached and transported to the lower areas of a region, such as along the margins of drainage channels. As the Urucuia Group sandstones contain lower proportions of zircon and tourmaline and, taking into account the presence of ferricrete in outcrops mapped by Bueno (2012) at the Serra do Espírito Santo, the high concentrations of eTh and eU observed on the

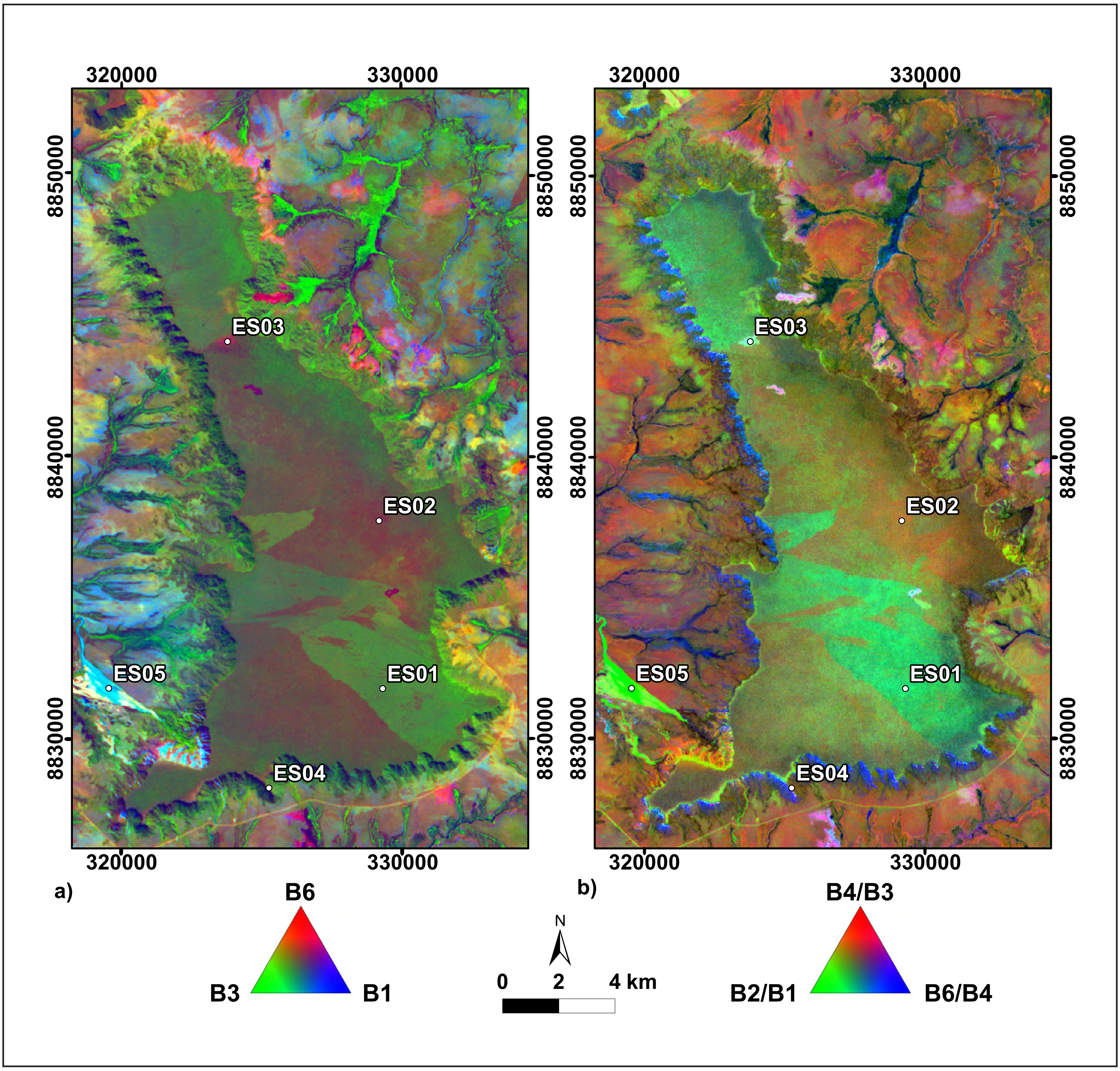

FIGURE 12 – RGB composite color pattern for ASTER sensor images. a) Individual bands (B6, B3, and B1). b) Ratios (B4/B3, B2/B1, and B6/B4). ES01 – ES05 are locations on the spectral profiles.

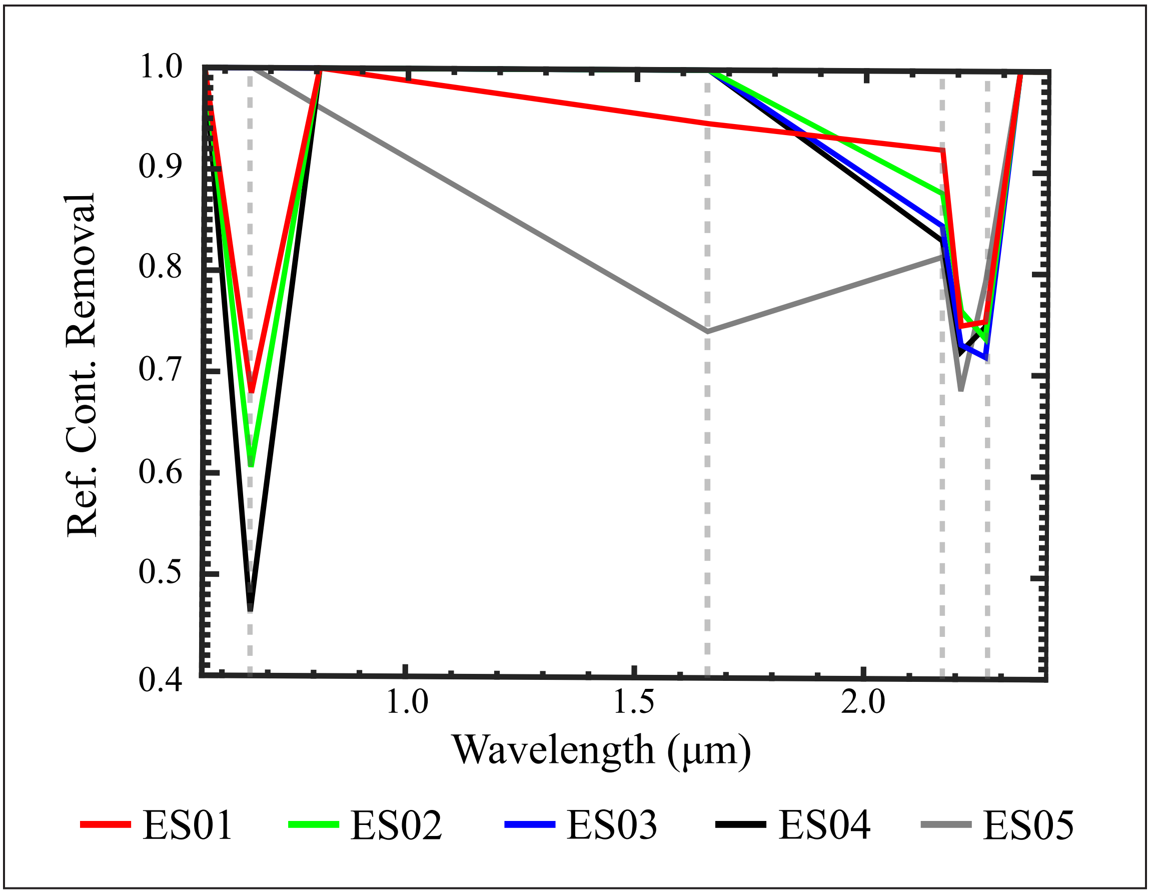

FIGURE 13 – Spectral profiles of pixels located in the Serra do Espirito Santo and in its surroundings. The dashed vertical lines indicate the absorption features described in Table 3.

TABLE 3: Summary of main characteristics observed in the ASTER sensor images over the areas represented by ES01 and ES05 points.

Points	Main absorption features (μm)	RGB individual bands	RGB band ratios
ES01	0.66 e 2.17 – 2.21	Olive green	Aqua green
ES02	0.66 e 2.17 – 2.21	Brown/ light brown	Orange
ES03	2.17 – 2.21	Reddish brown	Cyan/light blue
ES04	0.66 e 2.17 – 2.21	Brown/dark brown	Grayish brown
ES05	1.66 e 2.17 – 2.21	Cyan	Lemon green

residual landforms can be related to the occurrence of these accessory materials.

The low radioelements concentration on the Jalapão Surface can be explained by the presence of sediments derived from source rock (sandstone), weathering materials, and/or soils components. It has not been possible yet to interpret the reason for the K concentration observed in the eastern portions of residual landforms, near Mateiros and São Félix do Tocantins. Although such concentrations could be caused by alluvial deposits containing K-bearing minerals (Bierwirth 1996; Pickup and Marks 2000), we do not have sufficient information to explain these elevated K occurrences and, consequently, why they occur only in the eastern portions of residual landforms.

Thorium and U adsorbed on phyllosilicate minerals, such as illite, montmorillonite or kaolinite, may also contribute to the increase in the equivalent concentrations of these elements at the top of residual landforms (Megumi and Mamuro 1977; Taylor et al. 2002; Wilford and Minty 2007). And the presence of argillaceous materials could also explain the increase in K concentration at the top of the ridges compared to the surrounding terrain, as K can also be adsorbed on clays or by Cationic Exchange Capacity (Mello et al. 2021; Sparks 1987; Wilford and Minty 2007). This is corroborated by the results of the RGB composite color analysis and the spectral profiles of the ASTER sensor bands (Figures 12 and 13).

The possibility to infer the presence of clay minerals through multispectral images is because many clay bear hydroxyl (OH) which produce absorption features in SWIR region (Hunt 1977). The iron oxide can be inferred by absorption features associated to Fe in VNIR region (Cloutis 1996; Goetz and Rowan 1981). In the context of weathered rock studies, it is hope that association between clay minerals and iron oxides can generate absorption features as VNIR well as SWIR regions. Furthermore, for weathered rock, hematite, goethite and kaolinite are the largest minerals that occur in sufficient quantities can be distinguished in remote sensing (Deller 2006).

Kaolinite has an absorption feature around 2.2 μm (Hunt 1979). In the RGB image of individual bands (B6, B3, and B1) and ratios (B4/B3, B2/B1, and B6/B4), kaolinite-rich zones are seen in shades of light blue (or cyan) and light green, respectively (Deller 2006). Bearing in mind such properties of kaolinite and considering the results of Table 3, the absorption features in the region between 2.17 – 2.21 μm identified in the profiles ES01 - ES05 can be interpreted as evidence for the presence of clay minerals, mainly, kaolinite. As ES01, ES02, ES03, and ES04 points occur at the top of Serra do Espirito Santo, and then it is possible that clay materials could be one of the sources of K concentrations. This fact is consistent with the observations of Bueno (2012) who had already described that the outcrops at ES04 point were more argillaceous than the other materials of the Urucuia Group. Unfortunately, it was not possible to know exactly which clay minerals are rich in K. However, it is known that the presence of micas and vermiculites in kaolinites can increase the affinity it for K+ (Sparks 1987). Therefore, we suggest that the K concentration seen on the residual landforms may be related to kaolinite, as well as other clay components.

Another interesting aspect is the intensity of the absorption feature at 2.21 μm along the spectral profiles. This value increases from the points located at the top (ES01, ES02 and ES03), to the point located in the surrounding (ES05), of Serra do Espírito Santo. The increase in absorption intensity towards the Jalapão dunes (ES05) suggests that OH-bearing mineral particles tend to accumulate at the base of Serra do Espírito Santo. This in fact occurs because the Jalapão dunes result from the disaggregation and deposition of sediments from the sandstones of Serra do Espírito Santo (Morais and Cristo 2015; Cristo and Robaina 2016).

The more intense absorption feature at ES05 point may explain why only the areas at this point present a pattern of shades expected for zones rich in kaolinite according to the RGB composite color, as proposed by Deller (2006). The patterns in the other profiles suggest the presence of other minerals besides kaolinite. For the ES01, ES02 and ES04 profiles, the reflectance with continuum removal curves indicate that Fe oxides/hydroxides, mainly hematite and goethite could be proportionally higher than at the kaolinite enriched top of Serra do Espírito Santo.

Hematite and goethite have their diagnostic features related to Fe3+ which, in turn, is characterized by diagnostic features in the regions close to 0.6 and 0.9 μm (Bishop 2019). In the RGB compositions proposed by Deller (2006) for the ASTER images, zones rich in hematite/goethite, such as ferricretes, are seen in brown/dark reddish brown (individual bands) and orange (ratios) tones.

The ES01, ES02 and ES04 spectral profiles show a strong absorption feature at 0.66 μm. The presence of ferruginous materials at ES04 point mapped by Bueno (2012) supports the hypothesis that this absorption feature is related to the Fe3+ content present in oxides/hydroxides at the top of Serra do Espirito Santo. Note that, although the ES01 reflectance curve has a similar behavior to the ES02 and ES04 profiles, the shade pattern of the former (green – olive/light green) is different from that of the latter two (brown/light brown/dark brown). This difference may be due to mixing of spectral signals from different minerals.

Special mention should be made of the ES03 spectral profile. It presents a reflectance with continuum removal curve similar to those for ES01, ES02 and ES04, but differs from them by the absence of an absorption feature at 0.66 μm. It also differs from the profile for ES05, as the latter has an absorption feature at 1.66 μm. The shade pattern at ES03 also differs from those at ES01, ES02, ES04, and ES05, in terms of RGB composite colors (individual and ratio bands). These observations suggest that the Fe oxide/hydroxide content is lower in the areas represented by ES03 when compared to ES01, ES02 and ES04, but the clay content could be similar. The clay content at ES03 is probably lower than that at ES05, as this point has the highest absorption feature at 2.17 – 2.21 μm.

At least two possible explanations for the situation at ES03 can be suggested: i) The spectral responses and shade patterns at ES03 result from a mixture of clay minerals and Fe oxides that is different from what is observed in the other profiles. ii) In addition to clay minerals and Fe oxides, it is possible that another mineral species could be present at ES03. It is recommended to carry out field research in the region to evaluate these possibilities. It has not been possible so far to interpret the absorption feature at 1.66 μm that occurs only in the spectral profile at ES05. It is possible that this feature is related to the water content present in the atmosphere, since the region between 1.4 and 1.9 μm is obscured due to atmospheric absorption, mainly due to the presence of features produced by vibrations derived from the rotation of water and carbon dioxide molecules (Hunt 1979).

In agreement with findings on radiometric maps and ASTER images, the respective residual landforms and dissected surfaces can be distinguished on magnetic maps as well. However, it should be noted that while the products derived from gamma-spectrometry and ASTER sensors are related to surface processes, magnetic data provide information on subsurface magnetic susceptibility contrasts.

The presence of hematite/goethite may be related to the eTh and eU concentrations, but this may not explain the magnetic anomalies associated with the residual landforms, as both hematite and goethite are only weakly magnetic (e.g., Clark 1997; Dauth 1997). In lateritic soils, the main magnetic minerals are magnetite and maghemite (Singer et al. 1996; Mullins 1997). It is possible that magnetite/maghemite contribute to the magnetic signals associated with residual landforms. However, aerial surveys with a nominal flight height of 100 m generally do not provide sufficient resolution to identify the magnetic signal contributions from the alteration mantle (Dauth 1997). Furthermore, our depth estimates for the magnetic sources over the study region suggest that they are located at considerable depth.

SEDS estimates demonstrate that the sources of magnetic anomalies associated with residual landforms are located at depths up to 400 m. As the greatest magnetization contrasts are located at the edges of the residual landforms, where the magnetic sources are best represented by contact zones, such solutions may be quite imprecise, as they should be calculated with $\eta = 0$ and not with $\eta = 1$ (Reid and Thurston 2014). The software for SEDS calculation does not perform calculations for $\eta = 0$. On the other hand, depth values less than 400 m have also been observed based on VES analysis in the Occidental Bahiano Plateau (Gaspar 2006). The agreement between the depth values obtained by VES (≈ 270 m) and the average depth of the S3 magnetic source ensemble (≈ 0.27 km) suggests that the sources of the magnetic anomalies associated with the residual landforms must be positioned into the lower Urucuia Group.

Although the base of the Urucuia Group (Posse Formation) contains ferruginous cementation, this is more intense in the Serra das Araras Formation. If we consider that the sources of magnetic anomalies associated with residual landforms are located at average depths of ≈ 270 m and that the difference in elevation of the top of residual landforms and the floor of dissected surfaces (Jalapão Surface) is between 270 m and 298 m, then the sources of these magnetic anomalies coincide with the Fe oxide-rich layers of the lower portion of the Serra das Araras Formation mentioned by Cristo et al. (2013) and Morais and Cristo (2015). The presence of ferrimagnetic minerals, however, is not mentioned in previous works, so it is not known if such minerals are present and if they occur in sufficient quantities to generate aerial magnetic anomalies.

Finally, the results allow us to rule out the possibility of basement structures as sources of magnetic anomalies associated with residual landforms, as the basement depth of the basin is estimated at ≈ 1.44 km, both by the depth estimate given by RAPS and by VES analysis. The average depth of the S1 ensemble (≈6.83 km) is associated with regional magnetic anomalies. We assume that the magnetic signal of this ensemble is due to the magnetic contrast of large-scale structures, such as the Alto do São Francisco and/or Transbrasiliano Lineament System, but, as it is not possible to know the spatial location of the sources based on the RAPS, this question remains unresolved.

6. Conclusions

This study was carried out to contribute to the understanding of the origin of airborne geophysical responses in the Jalapão region. Based on the interpretation of remotely sensed data, it was possible to characterize the main Jalapão geomorphological units and successfully point out probable sources of the geophysical responses. The gamma-ray signals likely derive from the soil cover on geomorphological units. Low-amplitude, high-frequency magnetic signals over residual landforms can be explained by the possible presence of ferrimagnetic minerals or of an alteration mantle (magnetite/maghemite), or ferruginous cements at the base of the Serra das Araras Formation sandstones. Although the real nature of the magnetic sources of these signals remains unknown, the results presented here allow us to state that the depth of such sources is shallow and that it is unlikely that they are related to the basement for which depth estimates of ≈ 1.44 km were obtained.

Acknowledgements

The authors of this study are grateful to the Brazilian National Agency of Petroleum, Natural Gas and Biofuels and Remote Sensing and Geophysics Division of the Geological Survey of Brazil for providing the airborne geophysical data that were used in this work. The authors are also grateful to Rafael Pires de Lima who helped review the manuscript and the JGSB's reviewers Luis Eduardo de Souza Robaina (Federal University of Santa Maria) and Wolf Uwe Reimold (University of Brasilia) for corrections and observations suggested which helped to improve the manuscript.

Authorship credits

Author	A	B	C	D	E	F
ABS	▨	▨	▨	▨	▨	▨
FMA		▨		▨	▨	

A - Study design/Conceptualization **B** - Investigation/Data acquisition
C - Data Interpretation/Validation **D** - Writing
E - Review/Editing **F** - Supervision/Project administration

Declaration of interests

The authors declare that they have no known competing financial interests or personal relationships that could have appeared to influence the work reported in this paper.

References

Amorim Junior V., Lima O.A.L. 2007. Avaliação hidrogeológica do aqüífero Urucuia na bacia do rio das Fêmeas - BA usando resistividade e polarização elétrica induzida. Revista Brasileira de Geofísica, 25(2), 117-129. https://doi.org/10.1590/S0102-261X2007000200002

Barbosa V.C.F., Silva J.B.C. 2005. Deconvolução de euler: passado, presente e futuro - um tutorial. Revista Brasileira de Geofísica, 23(3), 243-250. https://doi.org/10.1590/S0102-261X2005000300004

Benvindo R.A.F. 2009. Análise comparativa dos instrumentos de regulamentação das políticas de proteção ambiental e de promoção do ecoturismo: o caso do Parque Estadual do Jalapão – TO. MSc Dissertation, Faculdade de Arquitetura e Urbanismo, Universidade de Brasília, 201 p. Available online at: https://repositorio.unb.br/handle/10482/4328 / (accessed on 1 July 2022).

Bierwirth P. 1996. Investigation of airborne gamma-ray images as a rapid mapping tool for soil and land degradation - Wagga Wagga, NSW. Australian Geological Survey Organization, v. 22, 71 p. Available online at: https://ecat.ga.gov.au/geonetwork/srv/api/records/a05f7892-740e-7506-e044-00144fdd4fa6 / (accessed on 4 July 2022)

Bishop J. 2019. Visible and near-infrared reflectance spectroscopy: laboratory spectra of geologic materials. In: Bishop J., Bell III J., Moersch J. (eds.). Remote compositional analysis: techniques for understanding spectroscopy, mineralogy, and geochesmistry of planetary surfaces. Cambridge Planetary Science, p. 68-101. https://doi.org/10.1017/9781316888872.006

Bonfim L.F.C., Gomes R.A.D. 2004. Aquífero Urucuia – geometria e espessura: ideias para discussão. In: Congresso Brasileiro de Águas Subterrâneas, 13. Available online at: https://rigeo.cprm.gov.br/handle/doc/16649 / (accessed on 1 July 2022).

Bueno R.M. 2012. Interpretação paleoambiental de paleossolos do Grupo Urucuia (cretáceo superior). MSc Dissertation, Instituto de Geociências, Universidade Estadual de Campinas, 99 p. https://doi.org/10.47749/T/UNICAMP.2012.872485

Campos J.E.G., Dardenne M.A. 1997a. Estratigrafia e sedimentação da Bacia Sanfranciscana: uma revisão. Revista Brasileira de Geociências, 27(3), 269-282. https://doi.org/10.25249/0375-7536.1997269282

Campos J.E.G., Dardenne M.A. 1997b. Origem e evolução tectônica da Bacia Sanfranciscana. Revista Brasileira de Geociências, 27(3), 283-294. https://doi.org/10.25249/0375-7536.1997283294

Chang H.K., Bender A.A., Kowsmann R.O. 1992. O papel das tensões intraplaca na evolução de bacias sedimentares: exemplo da Formação Urucuia. In: Congresso Brasileiro de Geologia, 37, 568-569. Available on line at: http://www.sbgeo.org.br/home/pages/44#Anais%20de%20Congressos%20Brasileiros%20de%20Geologia

Clark R.N., Roush T.L. 1984. Reflectance spectroscopy: quantitative analysis techniques for remote sensing applications. Journal of Geophysical Research, 89 (B7), 6329-6340. https://doi.org/10.1029/JB089iB07p06329

Clark D.A. 1997. Magnetic petrophysics and magnetic petrology: Aids to geological interpretation of magnetic surveys. Journal of Australian

Geological and Geophysical, 17(2), 83-103. Available on line at: https://ecat.ga.gov.au/geonetwork/srv/api/records/fae9173a-71b4-71e4-e044-00144fdd4fa6 / (accessed on 4 July 2022)

Cloutis E.A. 1996. Hyperspectral remote sensing: evaluation of analytical techniques. International Journal of Remote Sensing, 17(12), 2215-2242. https://doi.org/10.1080/01431169608948770

Correa R.T. 2019a. Mapa radiométrico do Brasil. Escala 1:5.000.000. Brasília, CPRM. Available on line at: https://rigeo.cprm.gov.br/handle/doc/21296 / (accessed on 1 July 2022).

Correa R.T. 2019b. Mapa magnetométrico do Brasil. Escala 1:5.000.000. Brasília, CPRM. Available on line at: https://rigeo.cprm.gov.br/handle/doc/21299 / (accessed on 1 July 2022).

Cristo S.S.V., Robaina L.E.S., De Morais F. 2013. Patrimônio geomorfológico do leste do Estado do Tocantins: região do Jalapão. Geonomos, 21(2), 92-96. https://doi.org/10.18285/geonomos.v21i2.276

Cristo S.S.V., Robaina L.E.S. 2016. Análise geomorfológica em Unidades de Conservação da Natureza: Estação Ecológica Serra Geral do Tocantins – estados do Tocantins e da Bahia. Ateliê Geográfico, 10(3), 73-88. https://doi.org/10.5216/ag.v10i3.31162

Dauth C. 1997. Airborne magnetic, radiometric and satellite imagery for regolith mapping in the Yilgard Craton of Western Australia. Exploration Geophysics, 28(1-2), 199-203. https://doi.org/10.1071/EG997199

Deller M.E.A. 2006. Facies discrimination in laterites using Landsat Thematic mapper, ASTER and ALI data – examples from Eritrea and Arabia. International Journal of Remote Sensing, 27(12), 2389-2409. https://doi.org/10.1080/01431160600586050

Durrheim R.J., Cooper G.R.J. 1998. EULDEP: a program for the Euler deconvolution of magnetic and gravity data. Computers and Geoscience, 24(6), 545-550. https://doi.org/10.1016/S0098-3004(98)00022-3

Dutra V., Colares A., Adorno L. F. M., Magalhães K., Gomes K. 2008. Proposta de estradas-parque como unidade de conservação: dilemas e diálogos entre o Jalapão e a Chapada dos Veadeiros. Sociedade & Natureza, 20(1), 161-176. https://doi.org/10.1590/S1982-45132008000100011

ENVI. 2009. Atmospheric correction module: QUAC and FLAASH User’s Guide. Version 4.7, ITT Visual Information Solutions, 44 p. Available online at: https://www.l3harrisgeospatial.com/portals/0/pdfs/envi/Flaash_Module.pdf / (accessed on 1 July 2022).

Fujisada H. 1998. ASTER Level-1 data processing algorithm. IEEE Transaction on Geoscience and Remote Sensing, 36 (4), 1101-1112. https://doi.org/10.1109/36.700994

Gaspar M.T.P. 2006. Sistema Aquífero Urucuia: caracterização regional e propostas de gestão. PhD Thesis, Instituto de Geociências, Universidade de Brasília, 204 p. Available online at: https://repositorio.unb.br/handle/10482/6742 / (accessed on 1 July 2022).

Gaspar M.T.P., Campos J.E.G., Moraes R.A.V. 2012. Determinação das espessuras do Sistema Aquífero Urucuia a partir de estudo geofísico. Revista Brasileira de Geociências, 42 (suppl. 1), 154-166. http://dx.doi.org/10.5327/Z0375-75362012000500013

Serviço Geológico do Brasil - CPRM. 2021. GeoSGB (Database): dados, informações e produtos do Serviço Geológico do Brasil. Serviço Geológico do Brasil - CPRM. Available on line at: http://geosgb.cprm.gov.br / (accessed 20 April 2021).

Goetz A.F.H., Rowan L.C. 1981. Geologic remote sensing. Science, 211(4484), 781-791. https://doi.org/10.1126/science.211.4484.781

Gonçalves R.D., Stollberg R., Weiss H., Chang H.K. 2020. Using GRACE to quantify the depletion of terrestrial water storage in Northeastern Brazil: the Urucuia Aquifer System. Science of the Total Environment, 705, 135845. https://doi.org/10.1016/j.scitotenv.2019.135845

Hunt G. R. 1977. Spectral signatures of particulate minerals in the visible and near infrared. Geophysics, 42(3), 501-513. https://doi.org/10.1190/1.1440721

Hunt G.R. 1979. Near-infrared (1.3–2.4 μm) spectra of alteration minerals – potential for use in remote sensing. Geophysics, 44 (12), 1974-1986. https://doi.org/10.1190/1.1440951

ICMBIO. 2013. Atlas do corredor ecológico da região do jalapão: 2ª versão. Projeto Corredor Ecológico da Região do Jalapão. Brasília, ICMBIO, 87 p. Available online at: https://www.icmbio.gov.br/projetojalapao/images/stories/atlas/AtlasJica_2013_COMPLETO.pdf / (accessed on 1 July 2022).

Kalinowski A., Oliver S. 2004. ASTER Mineral index processing manual. Canberra, Geoscience Australia, 37 p. Available online at: http://pid.geoscience.gov.au/dataset/ga/67973 / (accessed on 1 July 2022).

Kiang C.H., Silva F.P. 2015. Contribuição ao arcabouço geológico do sistema aquífero Urucuia. Geociências, 34(4), 872-882. Available online at: https://ppegeo.igc.usp.br/index.php/GEOSP/article/view/9037 / (accessed on 4 July 2022).

LP DAAC. 2020. ASTER Level 1 Precision Terrain Corrected Registered At-Sensor Radiance V003 [Data set]. NASA EOSDIS Land Processes DAAC. https://doi.org/10.5067/ASTER/AST_L1T.003

Li X. 2003. On the use of different methods for estimating magnetic depth. The Leading Edge, 22(11), 1090-1099. https://doi.org/10.1190/1.1634912

Li X. 2006. Understanding 3D analytical signal amplitude. Geophysics, 71(2), L13-L16. https://doi.org/10.1190/1.2184367

Marques R.P., Kassab Jr F., Molina E.C., Andrade F.A.R. (eds.). 2006. Levantamentos aerogeofísicos para a identificação de áreas com ocorrência potencial de petróleo e gás na Bacia do Parnaíba – Tomo II: área Parnaíba – aerolevantamento magnético e gamaespectrométrico. São Paulo, ANP-USP, 109 p. Available online at: https://reate.cprm.gov.br/arquivos/index.php/s/zTQ17CWbL2Wvx5f?path=%2FNAO_SISMICOS%2FMAGNETOMETRIA_GAMAESPECTROMETRIA%2F0050_MAGGAMA002 (accessed on 1 July 2022).

Megumi K., Mamuro T. 1977. Concentration of uranium series nuclides in soil particles in relation to their size. Journal of Geophysical Research, 10(2), 353-356. https://doi.org/10.1029/JB082i002p00353

Mello D.C., Demattê J.A.M., Mello F.A.O., Poppiel R.R., Silveiro N.E.Q., Safanelli J.L., Barros e Souza A., Di Raimo L.A.D.L., Rizzo R., Resende M.E.B., Schaefer C.E.G.R. 2021. Applied gamma-ray spectrometry for evaluating tropical soil processes and attributes. Geoderma, 381, 114736. https://doi.org/10.1016/j.geoderma.2020.114736

Mendes L.M. 2008. Aplicações de técnicas de geoprocessamento para análise geomorfológica do Parque Estadual do Jalapão (TO) e entorno. MSc Dissertation, Instituto de Ciências Humanas, Universidade de Brasília, 78 p. Available online at: https://repositorio.unb.br/handle/10482/4385 / (accessed on 1 July 2022).

Morais F., Cristo S.S.V. 2015. Jalapão: sedimentary heritages in central brazil. In: Vieira B., Salgado A., Santos L. (eds.). Landscapes and landforms of Brazil. World Geomorphological Landscapes. p. 191-200. https://doi.org/10.1007/978-94-017-8023-0_17

Mullins C.E. 1977. Magnetic susceptibility of the soil and its significance in soil science: a review. Journal of Soil Science, 28(2), 223-246, 1977. https://doi.org/10.1111/j.1365-2389.1977.tb02232.x

NCEI. 2021. Magnetic field calculators. Available online at: https://www.ngdc.noaa.gov/geomag/calculators/magcalc.shtml#igrfwmm / (accessed on 1 July 2022).

NATURATINS; Secretaria do Planejamento e Meio Ambiente – Tocantins. 2003. Plano de manejo do Parque Estadual do Jalapão. Palmas, 2003, 209 p. Available online at: http://gesto.to.gov.br/site_media/upload/gestao/documentos/Plano_de_Manejo_-_PEJ_-_Encarte_2_-_Planejamento.pdf / (accessed on 1 July 2022).

Pickup G., Marks A. 2000. Identifying large-scale erosion and deposition processes from airborne gamma radiometrics and digital elevation models in a weathered landscape. Earth Surface Processes and Landforms, 25(5), 535-557. https://doi.org/10.1002/(SICI)1096-9837(200005)25:5<535::AID-ESP91>3.0.CO;2-N

Reid A.B., Allsop J.M., Granser H., Millett A.J., Somerton I.W. 1990. Magnetic interpretation in three dimensions using Euler deconvolution. Geophysics, 55(1), 80-91. https://doi.org/10.1190/1.1442774

Reid A.B., Thurston J.B. 2014. The structural index in gravity and magnetic interpretation: errors, uses, and abuses. Geophysics, 79(4), 1JA-Z105. https://doi.org/10.1190/geo2013-0235.1

Reinhardt N., Hermann L. 2018. Gamma-ray spectrometry as versatile tool in soil science: a critical review. Journal of Plant Nutrition and Soil Science, 182(1), 9-27. https://doi.org/10.1002/jpln.201700447

Roest W.R., Verhoef J., Pilkington M. 1992. Magnetic interpretation using the 3-D analytic signal. Geophysics, 57(1), 116-125. https://doi.org/10.1190/1.1443174

Sgarbi G.N.C., Sgarbi P.B.A., Campos J.E.G., Dardenne M.A., Penha U.C. 2001. Bacia Sanfranciscana: o registro fanerozóico da Bacia do São Francisco. In: Pinto C.P., Martins Neto M.A. (eds). Bacia do São Francisco: geologia e recursos Naturais. Belo Horizonte, SBG MG. p. 93-138.

Silva A.B., Alves F.M. 2021. Atlas aerogeofísico do Estado do Tocantins. Goiânia, CPRM, 87 p. Available online at: https://rigeo.cprm.gov.br/handle/doc/22566 / (accessed on 1 November 2022).

Singer M.J., Verosub K.L., Fine P., Tenpas J. 1996. A conceptual model for the enhancement of magnetic suscetibility in soil. Quarternary International, 34-36, 243-248. https://doi.org/10.1016/1040-6182(95)00089-5

Sparks D.L. 1987. Potassium dynamics in soils. In: Stewart B.A. (ed.). Advances in soil science. Advances in Soil Science, 6, 1-63. https://doi.org/ 10.1007/978-1-4612-4682-4_1

Spector A., Grant F.S. 1970. Statistical models for interpreting aeromagnetic data. Geophysics, 35(2), 197-359. https://doi.org/10.1190/1.1440092

Spigolon A.L., Alvarenga C.J. 2002. Fácies e elementos arquiteturais resultantes de mudanças climáticas em um ambiente desértico: Grupo Urucuia (Neocretáceo), Bacia Sanfranciscana. Revista Brasileira de Geociências, 32(4), 579-586. Available on line at: https://www.ppegeo.igc.usp.br/index.php/rbg/article/view/9855 / (accessed on 1 July 2022).

Tschiedel M.W. 2004. Aplicação de estudo geofísico como contribuição ao conhecimento da tectônica da Sub-Bacia Urucuia. MSc Dissertation, Instituto de Geociências, Universidade de Brasília, 101 p. Available online at: http://mw.eco.br/ig/posg/mest/Mest185/mest185.pdf (accessed on 4 July 2022).

Taylor M.J., Smettem K., Pracillo G., Verboom W. 2002. Relationships between soil properties and high-resolution radiometrics, central eastern Wheatbelt, Western Australia. Exploration Geophysics, 33(2), 95-102. https://doi.org/10.1071/EG02095

Turkington A.V., Phillips J.D., Campbell S.W. 2005. Weathering and landscape evolution. Geomorphology, 67(1-2), 1-6. https://doi.org/10.1016/j.geomorph.2004.08.013

Vaz P.T.; Rezende N.G.A.M., Wanderley Filho J.R., Travassos W.A.S. 2007. Bacia do Parnaíba. Boletim de Geociências da Petrobrás, 15 (2), 253-263.

Vieira B.C., Salgado A.A.R., Santos L.J.C. 2015. Brazil: a land of beautiful and undiscovered landscapes. In: Vieira B., Salgado A., Santos L. (eds.). Landscapes and landforms of Brazil. Springer, p. 3-7. https://doi.org/10.1007/978-94-017-8023-0_1

Villela F.N.J, Nogueira C. 2011. Geologia e geomorfologia da estação ecológica Serra Geral do Tocantins. Biota Neotropica, 11(1), 217-229. https://doi.org/10.1590/S1676-06032011000100023

Thompson D. T. 1982. EULDPH: a new technique for making computer assisted depth estimates from magnetic data. Geophysics, 47(1), 31-37. https://doi.org/10.1190/1.1441278

Wilford J., Minty B. 2007. The use of airborne gamma-ray imagery for mapping soils and understanding landscape processes. In: Legacherie P., McBratney A.B., Voltz M. (eds.). Developments in soil science, 31, 207-218. https://doi.org/10.1016/S0166-2481(06)31016-1